Swift heavy ion irradiation of water ice from MeV to GeV energies : Approaching true cosmic ray compaction

E. Dartois, J. J. Ding, A. L.F. de Barros, P. Boduch, R. Brunetto, M. Chabot,
A. Domaracka, M. Godard, X. Y. Lv, C. F. Mejía Guamán, et al.

Astronomy
&
Astrophysics

Swift heavy ion irradiation of water ice from MeV to GeV energies

Approaching true cosmic ray compaction⋆

E. Dartois[1,2], J. J. Ding[3], A.L.F. de Barros[4], P. Boduch[3], R. Brunetto[1,2], M. Chabot[5,6], A. Domaracka[3],
M. Godard[7,1,2], X. Y. Lv[3], C. F. Mejía Guamán[8], T. Pino[9], H. Rothard[3], E. F. da Silveira[8], and J. C. Thomas[10]

[1] CNRS-INSU, Institut d'Astrophysique Spatiale, UMR 8617, 91405 Orsay, France
    e-mail: emmanuel.dartois@ias.u-psud.fr
[2] Université Paris Sud, Institut d'Astrophysique Spatiale, UMR 8617, bâtiment 121, 91405 Orsay, France
[3] Centre de Recherche sur les Ions, les Matériaux et la Photonique (CEA/CNRS/ENSICAEN/Université de Caen-Basse Normandie),
    CIMAP – CIRIL – Ganil, Boulevard Henri Becquerel, BP 5133, 14070 Caen Cedex 5, France
[4] Physics Departament, Centro Federal de Educação Tecnológica Celso Suckow da Fonseca, Av. Maracanã 229,
    20271-110 Rio de Janeiro, RJ, Brazil
[5] CNRS-IN2P3, Institut de Physique Nucléaire d'Orsay, UMR8608, 91406 Orsay, France
[6] Université Paris Sud, Institut de Physique Nucléaire d'Orsay, UMR8608, IN2P3-CNRS, bâtiment 103, 91406 Orsay, France
[7] NASA Goddard Space Flight Center, Greenbelt, MD 20771, USA
[8] Physics Departament, Pontifícia Universidade Católica do Rio de Janeiro, Rua Marquês de São Vicente 225,
    22451-900 Rio de Janeiro, RJ, Brazil
[9] Institut des Sciences Moléculaires d'Orsay, CNRS, UMR 8214, Université Paris Sud, 91405 Orsay, France
[10] Grand Accélérateur National d'Ions Lourds, CEA/DSM-CNRS/IN2P3, Boulevard Henri Becquerel, BP 55027,
    14076 Caen Cedex 5, France

ABSTRACT

Context. Cosmic ray ion irradiation affects the chemical composition of and triggers physical changes in interstellar ice mantles in space. One of the primary structural changes induced is the loss of porosity, and the mantles evolve toward a more compact amorphous state. Previously, ice compaction was monitored at low to moderate ion energies. The existence of a compaction threshold in stopping power has been suggested.
Aims. In this article we experimentally study the effect of heavy ion irradiation at energies closer to true cosmic rays. This minimises extrapolation and allows a regime where electronic interaction always dominates to be explored, providing the ice compaction cross section over a wide range of electronic stopping power.
Methods. High-energy ion irradiations provided by the GANIL accelerator, from the MeV up to the GeV range, are combined with in-situ infrared spectroscopy monitoring of ice mantles. We follow the IR spectral evolution of the ice as a function of increasing fluence (induced compaction of the initial microporous amorphous ice into a more compact amorphous phase). We use the number of OH dangling bonds of the water molecule, i.e. pending OH bonds not engaged in a hydrogen bond in the initially porous ice structure as a probe of the phase transition. These high-energy experiments are combined with lower energy experiments using light ions (H, He) from other facilities in Catania, Italy, and Washington, USA.
Results. We evaluated the cross section for the disappearance of OH dangling bonds as a function of electronic stopping power. A cross-section law in a large energy range that includes data from different ice deposition setups is established. The relevant phase structuring time scale for the ice network is compared to interstellar chemical time scales using an astrophysical model.
Conclusions. The presence of a threshold in compaction at low stopping power suggested in some previous works seems not to be confirmed for the high-energy cosmic rays encountered in interstellar space. Ice mantle porosity or pending bonds monitored by the OH dangling bonds is removed efficiently by cosmic rays. As a consequence, this considerably reduces the specific surface area available for surface chemical reactions.

Key words. cosmic rays – dust, extinction – ISM: molecules – line: profiles – molecular processes

1. Introduction

Icy mantles covering interstellar dust grains are present in the molecular clouds of our galaxy. These astrophysical environments are exposed to cosmic rays and ultraviolet photon irradiations, leading to a complex chemical evolution of matter that can be simulated in the laboratory for a better understanding of astrophysical processes. Numerous publications have reported ion bombardment experiments of interstellar ice analogues (e.g. Palumbo et al. 2008; Hudson & Moore 2001). However, these experiments are mainly performed at ion energies of 1 MeV or below, most of them involving irradiations with protons or light elements. There have been few experimental simulations of the irradiation by the high-energy cosmic ray component (just below or above 100 MeV/u, e.g. Seperuelo et al. 2009). Nevertheless, there is a clear need to study the interaction of high-energy

cosmic rays with interstellar ices since their energy deposit on dust grains and ice mantles is expected to be significant.

Often overlooked with respect to chemical modification by radiolysis, the physical state of water ice is also extremely important in many ways for astrophysicists, to allow surface physicists, for example, to perform experiments on realistic surfaces for a better understanding of interstellar chemistry, and in particular of hydrogen molecule formation. The physical state of ice (amorphous, crystalline, metastable) results from the interactions with ions, photons, and surface reactions (e.g. Palumbo et al. 2010; Accolla et al. 2011). It has been shown experimentally using low-energy ion irradiation that the astrophysically relevant low-temperature porous amorphous ice phase (called amorphous solid water, ASW) obtained by accretion of water molecules at 10–15 K is compacted under keV hydrogen irradiation, and evolves towards a compact non-porous but still disordered amorphous phase (e.g. Palumbo 2006 and article citations). When performing the experiment with crystalline water ice annealed at high temperature (above the cubic to hexagonal ice phase transition) and cooled down to 10 K, the ice structure is amorphized toward this same intermediate amorphous phase when exposed to similar beams (e.g. Baratta et al. 1991; Famá et al. 2010, and references therein). In this article we focus on higher energy and heavy swift ion irradiations of water-ice mantles, complemented by low-energy data. The experiments are described below (Sect. 2), followed by a description of the results (Sect. 3) and in particular the amorphous phase compaction cross-section dependance in a large energy deposition range. These measurements are relocated in an astrophysical context (Sect. 4) and open a discussion. A conclusion is drawn in Sect. 5.

2. Experiments

Swift ion irradiation experiments were performed at the heavy-ion accelerator Grand Accélérateur National d'Ions Lourds (GANIL[1], Caen, France). Heavy ion projectiles were delivered on the IRRSUD, SME, and LISE beam lines between July 2008 and June 2012 (the details are given in Table 1). These beams were coupled to the CASIMIR (Chambre d'Analyse par Spectroscopie Infrarouge des Molécules IRradiées) facility, a high vacuum chamber (10^{-7} mbar range) holding an infrared transmitting substrate cryocooled at 10 K, on top of which an amorphous ice film was condensed. Details of the experimental setup are given in Melot (2003). The ice films are produced by placing the cold window substrate in front of a deposition line. The film thickness is chosen to give a high band contrast with respect to the infrared absorption, without saturating the bands. The thickness is tailored to allow the ion beam to pass through the film with an almost constant energy deposition. A Nicolet FTIR spectrometer (Magna 550) with a spectral resolution of 1 cm^{-1} was used to monitor the infrared film transmittance. The evolution of the spectra was recorded at several fluences.

3. Results

Low-temperature vapour deposited ice is a non-relaxed solid, with a high microporosity, as revealed by the OH dangling bonds (OH-db) infrared signatures (with peak positions around 3695 and 3720 cm^{-1}, Fig. 1). It can adsorb large quantities of gases because of its open porosity. A variety of names for amorphous
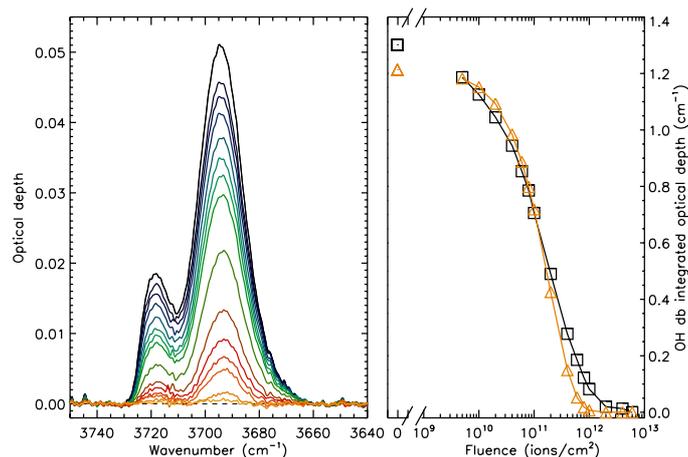
Fig. 1. *Left*: OH dangling bond baseline corrected absorbance spectra for different Ne^{6+} irradiation fluences (from top to bottom: 0, 5, 10, 20, 40, 60, 80, 100, 200, 400, 600, 800, 10^3, 2×10^3, 4×10^3, 6×10^3 in units of 10^9 ions/cm^2). The two bands at about 3720 and 3695 cm^{-1} correspond to 2- and 3-coordinated water molecules, respectively (see Sect. 4.3 for details). *Right*: evolution of the OH-db integrated absorbance as a function of the fluence (squares) and corresponding fitted exponential decay law (triangles).

ice are used in the literature to describe various formation pathways, but many of them are just similar ice prepared in different ways (Loerting et al. 2011). Our cryo-deposited films correspond to a microporous amorphous solid water (p-ASW), whose more generic name can be described by the (microporous) low-density amorphous ice (p-LDA) phase. The p-LDA is the bulk amorphous phase resulting from the annealing of very low-temperature vapour deposited cryofilms with a density of about 0.94 g/cm^3.

Upon ion irradiation, the disappearance of the OH-db is the most visible proof of the ice network change when starting with p-LDA ice. The evolution of the spectra and OH-db integrated optical depth with fluence are shown in Fig. 1 for the Ne^{6+} ion experiment. The integration is performed over the 3660 to 3730 cm^{-1} range after a spline baseline, fitted on the continuum on each side, has been subtracted. The evolution of the OH-db intensities as a function of the dose[2] for all the experiments we performed are shown in Fig. 2. For each experiment, the evolution of the OH dangling bonds integrated absorbance I with the ion fluence ϕ [ion/Å^2] is fitted by an exponential decay related to the ion effective OH-db destruction cross section $\sigma(Se)$ [Å^2]: $I(\phi, Se) = I_0 . \exp(-\sigma(Se)\phi)$. The corresponding energy deposition Se for a given ion is evaluated using the SRIM code (Ziegler et al. 2010).

The results for the dangling bonds destruction cross sections are displayed in Fig. 3 as a function of electronic stopping power Se. Additional measurements have been added for light ions at lower ion energies: data for 200 keV H$^+$ from Palumbo (2006), for 200 keV He$^+$, kindly provided from the Catania group by G. Strazzulla (see also Gomis et al. 2004) and for 800 keV H$^+$ by Marla Moore from NASA GSFC in Greenbelt, MD (see also Moore & Hudson 2000). The OH-dB destruction monitoring as a function of fluence was not the initial goal for the 200 keV He$^+$ and 800 keV H$^+$ light ions experiments. Therefore, a lower

[2] The dose is the dose deposited in the ice in eV/molecule, calculated using the SRIM/TRIM program, and assuming an amorphous ice density of 0.94 g/cm^3.

Table 1. Summary of experiments.

Ion	E_{In}[a] (MeV)	E_{Out} (MeV)	Se_{In}[b] (eV/Å)	ΔSe[b] (%)	Sn/Se_{In}[c] ($\times 10^{-3}$)	Ice film thickness[d] (μm)	Projected range[e] (μm)	σ[f] (10^4 Å^2)	Reference /measurement date
H$^+$	0.2	0.183	6.05	−5.5	1.29	0.25	3	0.0413 ± 0.02	Palumbo (2006)
H$^+$	0.8	0.727	2.57	−6.6	0.93	2.56	20	$0.0440^{+0.033}_{-0.02}$	Moore[g]
He$^+$	0.2	0.153	14.5	13.1	6.96	0.34	2.2	$0.0785^{+0.07}_{-0.02}$	Strazzulla[h]
Fe^{25+}	3640	3639	62.85	−0.02	0.42	1.5	3.4×10^3	1.6 ± 0.8	This work/29-08-2011
Ne^{6+}	19.6	17.7	143.1	−2.6	1.24	1.35	16.1	5.3 ± 1.2	This work/08-06-2012
Zn^{26+}	606	604	305.3	0.2	0.64	0.64	160	8.0 ± 1.4	This work/25-11-2010
Ni^{13+}	45.8	40.4	464.7	0.6	3.10	1.1	19.3	16 ± 6	This work/03-07-2008
Ta^{24+}	81	71	793.5	6.1	15.9	1.4	20.3	18.4 ± 4.1	This work/22-09-2011
Xe^{24+}	91.5	82	804.2	2.8	6.55	1.1	21.2	32 ± 15	This work/29-08-2008

Notes. [a] In: ion energy impinging the ice film, Out: energy calculated after crossing the ice film; [b] Se_{In} is the electronic stopping power at the ice film entrance and $\Delta Se = 100 \times (Se_{\text{In}} - Se_{\text{Out}})/Se_{\text{In}}$ the difference with the ice film exit electronic stopping power, respectively. The values are based on SRIM/TRIM calculations for pure ice. The absolute scale errors are dominated by the uncertainty for the density considered for the amorphous ice (0.94 g/cm^3) and the intrinsic uncertainties of the cross sections in SRIM/TRIM. [c] Sn refers to the nuclear stopping power. [d] approximate thickness assuming an integrated absorption cross section of 2×10^{-16} cm/molecule for the ice stretching mode. [e] calculated for a hypothetical semi-infinite ice target. [f] OH-db destruction (porosity loss) cross section. [g] 800 keV H$^+$ data provided by Marla Moore from NASA GSFC in Greenbelt, MD (see also Moore & Hudson 2000). [h] 200 keV He$^+$, data provided from the Catania group by G. Strazzulla (see also Gomis et al. 2004).
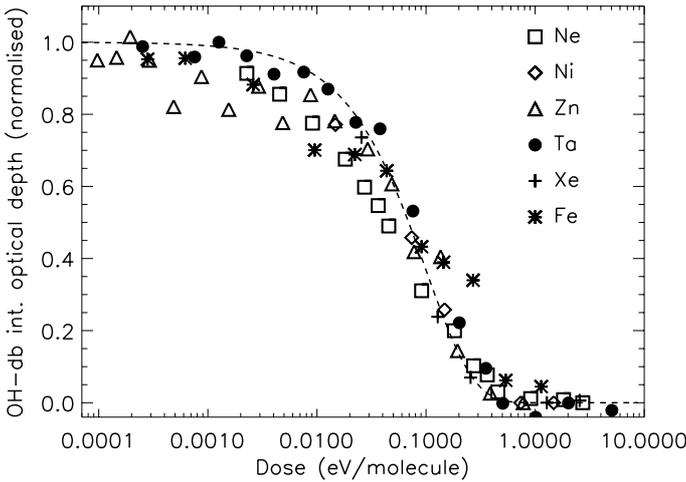
Fig. 2. Evolution of the integrated optical depth of the dangling bonds as a function of the dose for the experiments performed (the different symbols correspond to the various projectiles whose parameters are detailed in Table 1). The dashed line correspond to an exponential decay law.

sampling at low fluences was used, and sets higher upper limits for the error bars (fixing the maximum cross section).

The OH-db destruction cross section dependence in Å^2 can be described by $\sigma^{\text{OH d.b.}}(Se) = \sigma_0^{\text{OH d.b.}} \times Se^\beta$, with $\sigma_0^{\text{OH d.b.}} = 131^{+170}_{-65}$ Å^3/eV and $\beta = 1.0 \pm 0.2$. The reverse of the cross-section slope gives a mean value for the energy density u required to eliminate the OH-dB, associated with the ice compaction. The measurements cover the range $u = 7.6^{+7.5}_{-4.3} \times 10^{-3}$eV/Å^3, i.e. about $0.24^{+0.24}_{-0.1}$ eV/molecule at a density of 0.94 g/cm^3, which is comparable to the hydrogen bonding energy of ice around 0.2 to 0.3 eV/molecule (e.g. Isaacs et al. 1999; Brill & Tippe 1967). A dispersion with respect to a $\beta = 1$ slope for the cross section is observed. We emphasize that this scatter is most probably dominated by the variety of amorphous ice

produced within each setup, as revealed by the ratio of the initial OH-db integrated absorbance to another ice mode (e.g. libration, detailed in a forthcoming section). The extreme lower points from Catania were measured with an ice layer produced by background deposition, with a resulting initial porosity higher than for the GANIL experiments where a deposition line directed toward the substrate was used. This introduces a bias that has to be taken into account when comparing measurements from different laboratories, but it is also a chance to monitor the magnitude of the dependance on the initial dangling bonds density and the level of porosity. The errors of the absolute calibrations of fluences among laboratories that would slightly change the positions on the diagram are of lower amplitude than this effect.

4. Discussion

4.1. Other measurements of compaction

Infrared absorption spectroscopy was previously used by Palumbo (2006) to study the effects of ion irradiation on the microporosity of amorphous water ice. The OH dangling bond was monitored during irradiation with 200 keV protons at 15 K. The corresponding timescale for ice compaction by a distribution of cosmic rays was extrapolated and demonstrated to be shorter (a few millions years) than the estimated lifetime of dense clouds, above a few 10^7 years.

Raut et al. (2007a) used 100 keV Ar$^+$ ion irradiation to explore the difference in ultraviolet-visible spectroscopy, infrared spectroscopy, and methane adsorption/desorption techniques on the derived microporous ice compaction. They found that the decrease in internal surface area of the pores monitored via the dangling bonds in the infrared precedes the decrease in the pore volume during irradiation, monitored via the film thickness through interference fringes. The direct comparison with astrophysics is, however, difficult, as the 100 keV Ar$^+$ should, following SRIM calculations, deposit most of the energy in nuclear interactions (above 2/3 of it along the track), whereas electronic energy deposition dominates in the interstellar medium. In addition, the film thickness (4400 Å) is higher than the expected ion

projected range (by about a factor of 2) and thus the energy deposition is probably inhomogeneous, rendering the comparison less straightforward.

In a subsequent study, Raut et al. (2008) used a larger set of beams and focused on visible light spectroscopy coupled to a microbalance to further constrain the cross section for compaction. The derived cross section, lower than the corresponding Palumbo extrapolated one, gives more time to ice mantles to resist ion irradiation in space, but compaction still takes place on timescales comparable to a cloud's lifetime. However, about half of the ion beams used by Raut et al. (2008) suffer from a significant nuclear stopping power contribution and, thus, several kinds of interactions are mixed. The use of a 220 keV H$^+$ by Raut et al. and 200 keV H$^+$ by Palumbo offers the possibility to compare the cross section deduced with the two different techniques with similar stopping power, both dominated by electronic energy deposition. When the correction factor for the small energy difference is compensated, the dangling bond disappearance measured by Palumbo (2006) is about six to ten times faster than the porosity recorded using visible spectroscopy only.

The Palumbo (2006) experiment not only monitored the OH-db decrease but also the CO adsorption capabilities of the ice film. This technique, used in parallel to the IR spectra, shows that open porosity decreases faster than the expected compaction using the technique based on visible light by Raut et al. (2008). This open porosity defines the ability of small molecules to diffuse inside the amorphous ice pores, as probed by CO diffusion in the ice film (Palumbo 2006) and CH$_4$ uptake of the film (Raut et al. 2007a). The disappearance of OH dangling bonds implies a considerable reduction of the pores but does not necessarily imply that the resulting structure is a fully homogeneous compact planar film subsequent to the collapse of the pores. It seems reasonable that a reorganisation of the ice network at the deposited film scale (e.g. monitored by interference fringes and thickness modifications) will require a slightly higher total energy input than a local restructuring (that affects the local OH bonds). However, by monitoring the dangling bonds, we characterise the cross section to decrease the surface area of microporous ice, the most important factor for an efficient surface chemistry in space. In addition, this cross section is the only available observable for remote detection of ice porosity. One may thus use the term of open porosity loss as opposed to the compaction terminology. The first one may be more adapted to ice mantles in dense clouds, which are topologically different from planar thin films.

4.2. The existence of a threshold energy

Raut et al. (2008) suggested the occurrence of a stopping power threshold of 4 eV/Å to trigger the destruction of the open porosity of the ice. The existence of a minimum energy would increase the weight of the heavier ions in the process. In Sect. 4.3 we include this possibility to explore the expected variations of the open porosity decrease rates when considering an energy threshold. However the results presented in Fig. 3 do not seem to confirm the existence of a threshold with high-energy ions. The stopping power used to deduce the cross section dependence is the product of the macroscopic cross section and the average energy loss per collision, thus $-\frac{dE}{dx} = \mu Q_{\text{ave}}$, where $1/\mu$ is the mean free path between collisions and Q_{ave} the mean single-collision energy-loss spectrum at a molecular level. The mean free path of 1–10 MeV protons in water amounts to several tens to hundreds of Å. For the distributions of single event energy deposition
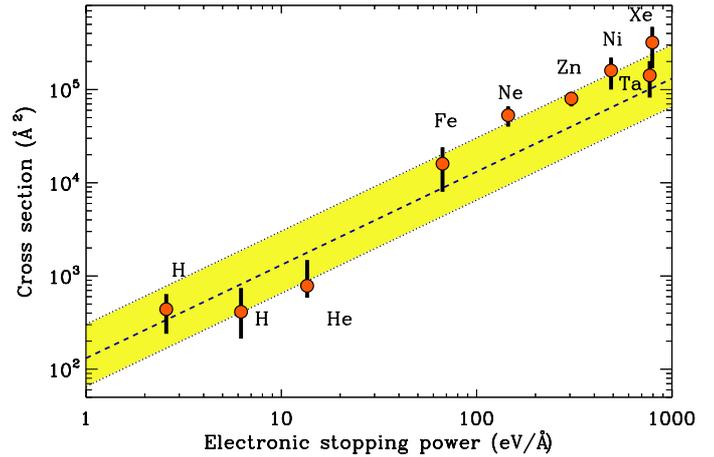
Fig. 3. Experimentally measured OH-db destruction (porosity loss) cross sections as a function of the stopping power in eV/Å. The dotted line corresponds to the best fit cross section and the yellow coloured zone defines the boundaries for the cross section curves ($\sigma^{\text{OH d.b.}}(Se_{[\text{eV}/\text{Å}]}) = 131^{+170}_{-65} Se^{1.0\pm0.2}_{[\text{eV}/\text{Å}]}$, see text for details).

with 1 MeV protons, ions, or electrons interacting with water or amorphous ice, the most probable ionisation (dominant process) energy loss is about 20 eV. The direct electronic excitation, dominated by the plasmon is around 21 eV. Both interactions are well above the previously mentioned threshold (e.g. Hamm et al. 1985; Pimblott et al. 1990; Dingfelder et al. 2000; Plante & Cucinotta 2008). The average energy lost per collision is higher than these values.

The energy deposition range where the probability distribution dominates the interactions is higher than the compaction threshold. It explains the efficient radiolysis of water observed with high-energy protons (e.g. production of H$_2$O$_2$, Moore & Hudson 2000), that would be difficult below the suggested stopping power threshold if the energy deposition per molecule was only a small fraction of an eV.

4.3. OH-db intensity and ice porosity

The higher and the lower frequency OH-db features shown in Fig. 1 have previously been assigned (Buch & Devlin 1991) to dangling bonds in 2- and 3-coordinated water molecules, respectively. The intensity of these modes, and the comparison to fundamental modes of ice can give some insight into the structure for the amorphous ice.

The variation in vibrational frequencies and absolute infrared absorption intensities in small-sized water clusters (Moudens et al. 2009, Fig. 5) help in determining the OH-db intensity. At the frequencies were the OH-db are observed, an intensity of about $50-100$ km/mole is expected, i.e. about $0.83-1.66 \times 10^{-17}$ cm/OH-db. Water dimer experiments (Kuyanov-Prozument et al. 2010) give 96 km/mole for the free donor OH-stretch band. These values are close to the gas phase value of 48 km/mole (Rothman et al. 2009). The strength of the libration mode (around 800 cm^{-1}) of the water ice is about 3.1×10^{-17} cm/H$_2$O (Gerakines et al. 1995), i.e 1.55×10^{-17} cm/OH, almost equal to or at most a factor of two higher than the OH-db. The ratio of these band integrated absorbances thus reflects the OH-dB fraction.

Table 2. Infrared Space Observatory observations.

Source	Right ascension	Declination	SWS template[a]	t_{int}[b] (s)	TDT[c]	Observation date
AFGL 989	06 41 10.1	09 29 35.8	1.3	3454	72602619	1997 Oct. 31
W33 A	18 14 39.4	–17 52 01.4	1.4	6538	32900920	1996 Oct. 10
	18 14 39.0	–17 52 04.0	6	7506	46700801	1997 Feb. 25
S140	22 19 18.2	63 18 47.6	1.4	6538	22002135	1996 Jun. 24
	22 19 18.2	63 18 47.2	6	5270	26301731	1996 Jul. 06
Elias 29	16 27 09.3	–24 37 21.1	1.3	3454	26700814	1996 Aug. 09
Elias 16	04 39 38.8	26 11 26.8	6	8682	68600538	1997 Oct. 01
RCrA IRS1	19 01 50.7	–36 58 9.9	1.4	6538	52301106	1997 Apr. 22

Notes. [a] Infrared Space Observatory, Short Wavelength Spectrometer (SWS) instrument observation template. [b] Observation total integration time. [c] Target dedicated time number of the observation.

Most of the experiments of direct ice deposition from water vapour on a cold substrate at low temperature presented here thus have about 0.5 to 1% of OH dangling bonds (the highest value corresponds to the background deposition, with a porosity of about 0.2). Higher relative intensities of dangling bonds (and thus higher porosities) can be obtained using experimental specific procedures, such as high inclination of the substrate window with respect to the water injection axis (e.g. Stevenson et al. 1999), or co-deposition with a rare gas that is eventually subsequently sublimated, leaving the pores free (e.g. Givan et al. 1996).

The relation between the measured porosity and the integrated optical depth of the dangling bonds seems to be almost linear, provided that the microporosity dominates. Using values in Table 1 from Raut et al. (2007b), we find that the porosity is approximately equal to the integrated optical depth of the dangling bonds when normalized to 10^{18} H_2O molecules.

Taking into account the OH-dB profile of Fig. 1, this translates into

$$\tau_{OH-dB} (3695 \text{ cm}^{-1}) \approx 1.9 \times 10^{-4} f_{porosity} \int_{band} OH_{3 \mu m} d\bar{\nu}$$
$$\approx 3.9 \times 10^{-2} f_{porosity} N_{H_2O} [10^{18} \text{ cm}^{-2}]$$
$$\text{with } 0 \leq f_{porosity} \leq 1.$$

Measurements using co-expansion with rare gases (Rowland & Devlin 1991) produce ice clusters whose size can be estimated from the ratio of the dangling surface modes to the bulk ice absorption.

When the situation in space is dominated by background deposition, i.e. that gas phase accretion contribution dominates, it leads to an intermediate porosity level (about 0.2). The experiments with the highest initial porosity, obtained by background deposition and corresponding to this space situation, translate into cross sections in the lower part of the range (Fig. 3) determined with $\sigma_0^{OH\,d.b.} \in [65-130]$ Å^3/eV. The formation of many species, including water, can proceed directly on the surface of grains (e.g. Oba et al. 2009; Dulieu et al. 2010) and thus does not enter stricto sensu to this regime. The initial degree of porosity when ices are produced by surface reactions in space is thus difficult to set, as they proceed on uneven irregular surfaces, are hardly reproducible in the laboratory, co-mixed with other species, are constantly desorbed by various energetic processes such as photodesorption, cosmic rays sputtering or eventually chemical reactions and subsequently frozen out (e.g. Hollenbach et al. 2009).

4.4. Astrophysical implications

4.4.1. Observations

Many articles discuss the presence of OH dangling bonds in astrophysical environments, but almost none compares them explicitly to astronomical spectra. There are only scarce observational constraints, where isolated OH dangling bonds are not observed (Keane et al. 2001). Many ground-based and satellite infrared spectra of young stellar objects exhibiting strong water-ice stretching mode absorption do exist, but the OH dangling bond spectral region is unobservable from the ground. The unique satellite that allowed this region to be observed is the Infrared Space Observatory. We retrieved Short Wavelength Spectrometer data (de Graauw et al. 1996) from the Infrared Space Observatory database[3] for some bright embedded sources with sufficient signal-to-noise ratios. The sources selected (Table 2) have different degrees of contribution from crystalline water ice arising in the most central regions of their surrounding dusty envelopes. Other sources, with higher signal-to-noise but clearly showing fully crystalline ice were excluded. In some cases (W33 A and S140), full resolution (SWS06) data were stitched to the available SWS01 observation template to benefit from the increase in signal-to-noise in the dangling bonds spectral region.

Optical depth spectra for the ice component were obtained from a continuum baseline subtraction of Infrared Space Observatory and are shown in Fig. 4. They are compared to laboratory spectra of pure H_2O and CO_2 ice, and a $H_2O:CO_2$ 12:1 mixture. The CO_2 and a $H_2O:CO_2$ laboratory spectra are normalised to the CO_2 column density observed with the antisymmetric stretching mode at 4.27 μm[4]. The H_2O dangling bond spectrum was normalized with the relation discussed in the preceeding section, assuming a porosity of 0.2, and integrating the OH stretching mode. In this way they can be directly compared. The result of this comparison is that the only absorptions emerging are combination modes of the CO_2 component present in the ice mantles of all these sources (see Keane et al. 2001, for a detailed discussion for S140), and no free OH dangling bonds are observed at the signal to noise level of the observations. The constraints are not always stringent for all the amorphous ice mantle line of sight observations, but contrast with the CO_2 combination modes that are detected. In the sequel, we compare this lack

---

[3] http://iso.esac.esa.int
[4] Using $A_{CO_2} = 7.6 \times 10^{-17}$ cm molecule^{-1} from Gerakines et al. (1995) for this mode, corresponding to $A_{CO_2} = 1.4 \times 10^{-18}$ cm molecule^{-1} for the $\nu_1 + \nu_3$ mode around 2.7 μm.
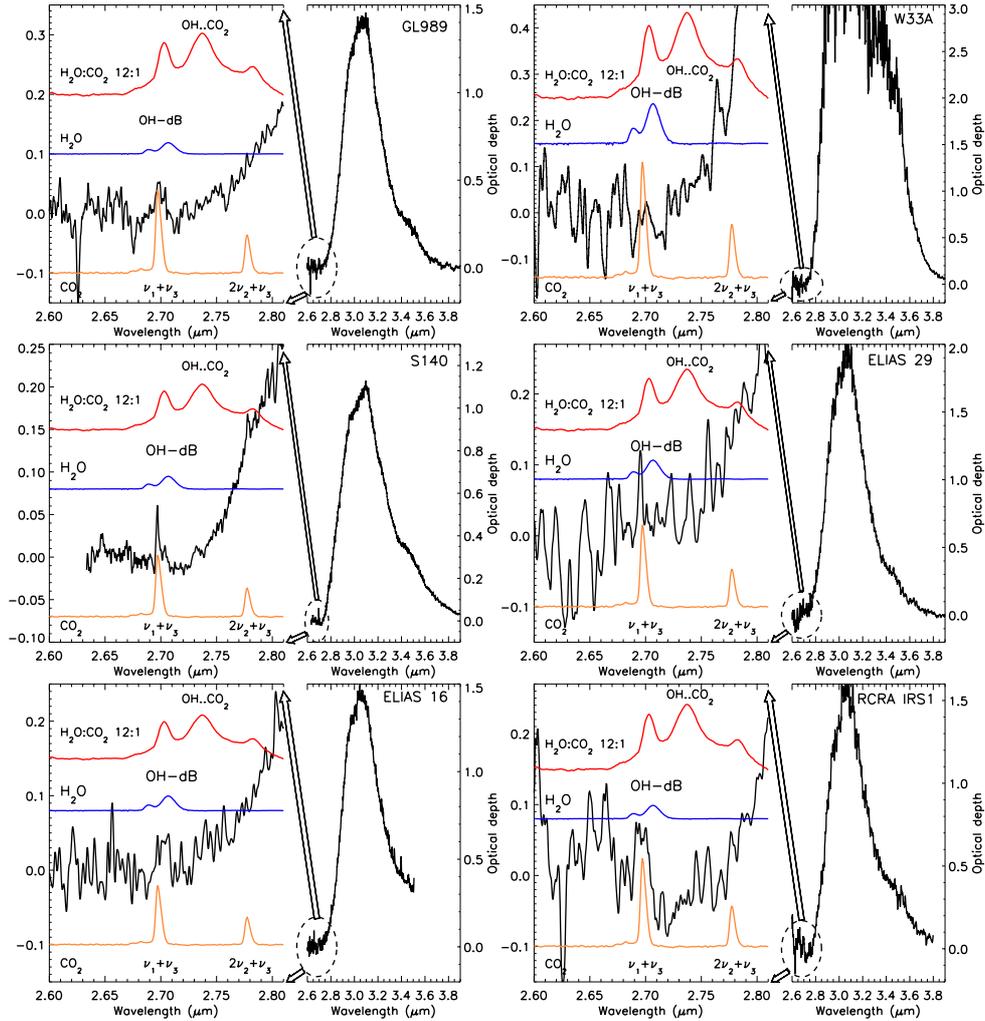
Fig. 4. Young stellar objects spectra measured with the Short Wavelength Spectrometer onboard the Infrared Space Observatory, compared to various laboratory ice mixtures recorded spectra. The optical depth astrophysical spectra are obtained from a continuum baseline subtraction. A close up on the dangling bond region is plotted in the left part of each panel. These spectra are compared to laboratory spectra of pure H_2O and CO_2 ice, and a $H_2O:CO_2$ 12:1 mixture. The CO_2 and a $H_2O:CO_2$ laboratory spectra are normalised to the CO_2 column density observed in the mid-IR. The H_2O dangling bond spectrum was normalized with the relation discussed in the preceeding section, assuming a porosity of 0.2, and integrating the OH stretching mode. See text for details.

of detection to the results of our calculations of the OH-dB destruction timescale.

4.4.2. Open porosity destruction timescale

Our cross section measurements can be used to infer the time scale τ for the loss of open porosity of ice mantles. This rate can be evaluated by integrating the product of this cross section with the cosmic ray flux over their energy and abundance distribution following

$$\tau^{-1} = 4\pi \sum_Z \int_{E_{\min}}^{\infty} \sigma^{OH\,d.b.}(E, Z) \frac{dN}{dE}(E, Z) dE \qquad (1)$$

where $\sigma^{OH\,d.b.}[\mathrm{cm}^2]$ is the loss of open porosity cross-section monitored by the OH dangling bonds, $\frac{dN}{dE}(E, Z)[\text{particles cm}^{-2}\,\text{s}^{-1}\,\text{sr}^{-1}/(\text{MeV/nucleon})]$ the differential flux of cosmic ray element of atomic number Z, with a cutoff in energy $E_{\min}$ set at 100 eV. The cross section $\sigma^{OH\,d.b.}(E, Z)$ is evaluated by combining the cross section $\sigma^{OH\,d.b.}(Se)$ established experimentally and the calculated electronic stopping cross section Se using the SRIM code

(Ziegler et al. 2010) as a function of atomic number Z and energy per nucleon E. For the differential flux we adopt the functional form given by Webber & Yushak (1983) also described in Shen et al. (2004)

$$\frac{dN}{dE}(E, Z) = \frac{C\, E_0^{0.3}}{(E + E_0)^3}, \qquad (2)$$

where C is a normalisation constant and E_0 a form parameter allowing one to account for the low-energy cosmic ray distribution.

The ionisation rate (ζ) corresponding to the same distribution can be calculated, and gives an observable comparison with astrophysical observations in various environments, essentially through H^{3+} ion observations (McCall et al. 2003; Dalgarno 2006; Geballe & Oka 2010; Indriolo & McCall 2012). Low-energy cosmic rays are less efficient in penetrating dense clouds, as diffuse interstellar medium rates are much higher than dense cloud rates. Indriolo & McCall (2012) have shown (their Fig. 19) a transition from a mean diffuse medium cosmic ray ionisation rate of $\zeta = 3.5^{+5.3}_{-3.0} \times 10^{-16}\,\text{s}^{-1}$ to ionization rates inferred in dense clouds a few times $10^{-17}\,\text{s}^{-1}$, i.e. approximately an order of magnitude lower. The form parameter E_0 applied to the differential

Table 3. OH-db destruction rates.

	GCR			$\odot$		
	$E_0 = 200$	$E_0 = 400$	$E_0 = 600$	$E_0 = 200$	$E_0 = 400$	$E_0 = 600$
$\zeta(\mathrm{s}^{-1})^a$	3.34(−16)	5.89(−17)	2.12(−17)	1.70(−16)	3.00(−17)	1.08(−17)
$E_{\mathrm{th}} = 0$ eV/Å^b						
Light^c	0.589	0.580	0.576	0.935	0.933	0.932
$Z \geq 3^d$	0.411	0.420	0.424	0.065	0.067	0.068
Fe	0.073	0.078	0.080	0.012	0.013	0.014
$\tau(\mathrm{My})^e$	0.14	0.71	1.82	0.25	1.34	3.48
$E_{\mathrm{th}} = 4$ eV/Å^b						
Light^c	0.122	0.090	0.075	0.534	0.455	0.410
$Z \geq 3^d$	0.878	0.910	0.925	0.466	0.545	0.590
Fe	0.179	0.213	0.238	0.101	0.139	0.168
$\tau(\mathrm{My})^e$	0.33	1.94	5.43	2.09	14.11	42.79

Notes. Calculated with the best fit cross section $\sigma^{\mathrm{OH\,d.b.}}(Se) = 131 \times Se(\mathrm{eV/Å})^{1.0}$. 4.05(−16) means 4.05×10^{-16}; $^{(a)}$ calculated ionisation rate; $^{(b)}$ adopted cross section stopping power threshold; $^{(c)}$ fraction of the OH-db destruction rate induced by H and He ions; $^{(d)}$ fraction of the OH-db destruction rate induced by Li to Ni ions; $^{(e)}$ OH-db calculated destruction time scale. A destruction time scale of one million years corresponds to a rate of about 3.17×10^{-14} s^{-1}.

flux of the cosmic rays allows the various observed ionization rates to be explored. The ionisation rate can be evaluated by replacing $\sigma^{\mathrm{OH\,d.b.}}$ by the ionisation cross section σ_{i}

$$\zeta = 4\pi \sum_Z \int_{E_{\min}}^{\infty} \sigma_{\mathrm{i}}(E, Z)(1 + \Phi_S(E, Z))\frac{\mathrm{d}N}{\mathrm{d}E}(E, Z)\mathrm{d}E \quad (3)$$

$$\approx 4\pi(1 + \eta) \int_{E_{\min}}^{\infty} \sigma_{\mathrm{p}}(E)(1 + \Phi_S(E, p))\frac{C\,E_0^{0.3}}{(E + E_0)^3}\mathrm{d}E, \quad (4)$$

where

$$\eta = \sum_{k \geq 2} \frac{f_k}{f_{\mathrm{p}}} Z_k^2 \quad (5)$$

is the factor to include the heavier elements' ionisation contribution (η); f_k is the fractional abundance of species k, A_k its number of nucleons, and Z_k its charge. The cross section for ionisation $\sigma_{\mathrm{p}}(E)$ is taken as the sum of the proton ionisation cross section (Rudd et al. 1985) and electron capture at low energies (Rudd et al. 1983) as in Padovani et al. (2009); $\Phi_S(E, Z)$ is the secondary electron contribution to the ionisation, taken from Glassgold & Langer (1973).

Two distributions of cosmic ray abundances are generally adopted in models: galactic cosmic rays (GCR) and, intriguingly, solar system (sol. syst.) abundance. The abundance of galactic cosmic rays adopted for H and He is from Wang et al. (2002), Li and Be from de Nolfo et al. (2006), and for elements above Be from George et al. (2009). For the solar system elemental abundances, we use a model distribution given by Lodders (2003) (Table 6). The distribution of cosmic rays impinging on a cloud should in principle be closer to the GCR distribution, but both are used in our modelling for comparison.

Table 3 summarizes the calculations with the determined open porosity decrease cross section. As expected from the distribution of elements, the contribution of heavier elements to the open porosity decrease rate is higher for GCR than for sol. syst. abundances. The deduced ionisation rates are also better reproduced by GCR. The existence of a threshold would not only further increase the relative heavy ion contribution, but also the timescale for open porosity disappearance by a factor of about 3

for GCR and up to 10 for sol. syst. distributions, suppressing the effect of most light elements.

The GCR distribution, combined with the cross section from the experiments presented in this article reproduces the ionisation rate and decreases the ice porosity in time scales of 1.4×10^5 to 2×10^6 years, depending on the adopted low-energy ions normalisation. This is in agreement with the observational constraints discussed above, where isolated OH dangling bonds are not observed.

5. Conclusion

We have studied the loss of open porosity of amorphous ice films submitted to high-energy ion irradiations in the MeV to GeV range. The probe transition of the phase evolution is the number of OH dangling bonds, i.e. pending water molecule OH bonds not engaged in a hydrogen bond in the initially porous ice structure. Combined with previous experiments using lower energy light ions from other facilities, we evaluated a cross section for the disappearance of porosity as a function of electronic stopping power in a three-decade range. The relevant phase structuring time scale for the ice network is compared to interstellar chemical time scales using an astrophysical model including the expected galactic cosmic ray distribution of abundances.

The main conclusions are:

– The experimentally measured variations in the open porosity loss cross section reflect the various initial porosities that have to be taken into account when comparing different laboratories' experiments.
– The previously suggested presence of a threshold in compaction at low stopping power for high-energy cosmic rays such as encountered in interstellar space seems not to be confirmed.
– The galactic cosmic ray distribution of ion abundances reproduces the ionisation rate observed and provides ice compaction time scales in the range from 1.4×10^5 to 2×10^6 years.
– Ice mantle porosity or pending bonds as monitored by the OH dangling bonds, are removed efficiently by cosmic rays.

Reactivity favoured by the large surface to volume ratio and many potential wells as measured using freshly deposited amorphous ice at low temperature can only be considered as upper limits to the reactivity encountered in astrophysical media. The consequence for astrochemistry is that it considerably reduces the specific surface area available for chemical reactions, lowering the surface chemistry rates.

References

Accolla, M., Congiu, E., Dulieu, F., et al. 2011, Phys. Chem. Chem. Phys. (Incorporating Faraday Transactions), 13, 8037

Baratta, G. A., Spinella, F., Leto, G., Strazzulla, G., & Foti, G. 1991, A&A, 252, 421

Brill, R., & Tippe, A. 1967, Acta Crystallogr. 23, 343

Buch, V., & Devlin, J. P. 1991, J. Chem. Phys., 94, 4091

Dalgarno, A. 2006, Proc. Nat. Acad. Sci., 103, 12269

de Graauw, T., Haser, L. N., Beintema, D. A., et al. 1996, A&A, 315, L49

de Nolfo, G. A., Moskalenko, I. V., Binns, W. R., et al. 2006, Adv. Space Res., 38, 1558

Dingfelder, M., Inokuti1, M., & Paretzke, H. G. 2000, Rad. Phys. Chem., 59, 255

Dulieu, F., Amiaud, L., Congiu, E., et al. 2010, A&A, 512, A30

Famá, M., Loeffler, M. J., Raut, U., & Baragiola, R. A. 2010, Icarus, 207, 314

Geballe, T. R., & Oka, T. 2010, ApJ, 709, L70

George, J. S., Lave, K. A., Wiedenbeck, M. E., et al. 2009, ApJ, 698, 1666

Gerakines, P. A., Schutte, W. A., Greenberg, J. M., & van Dishoeck, E. F. 1995, A&A, 296, 810

Givan, A., Loewenschuss, A., & Nielsen, C. J. 1996, Vib. Spectrosc., 12, 1

Glassgold, A. E., & Langer, W. D. 1973, ApJ, 186, 859

Gomis, O., Leto, G., & Strazzulla, G. 2004, A&A, 420, 405

Guillot, B., & Guissani, Y. 2004, J. Chem. Phys., 120, 4366

Hamm, R. N., Turner, J. E., Ritchie, R. H., & Wright, H. A. 1985, Radiat. Res. Suppl. 8, 20

Hollenbach, D., Kaufman, M. J., Bergin, E. A., & Melnick, G. J. 2009, ApJ, 690, 1497

Hudson, R. L., & Moore, M. H. 2001, J. Geophys. Res., 106, 33275

Indriolo, N., & McCall, B. J. 2012, ApJ, 745, 91

Isaacs, E. N., Shukla, A., Platzman, P. M., et al. 1999, Phys. Rev. Lett., 82, 600

Keane, J. V., Boogert, A. C. A., Tielens, A. G. G. M., Ehrenfreund, P., & Schutte, W. A. 2001, A&A, 375, L43

Kuyanov-Prozument, K., Choi, M. Y., & Vilesov, A. F. 2010, J. Chem. Phys., 132, 014304

Lodders, K. 2003, ApJ, 591, 1220

Loerting, T., Winkel, K., Seidl, M., et al. 2011, Phys. Chem. Chem. Phys. (Incorporating Faraday Transactions), 13, 8783

McCall, B. J., Huneycutt, A. J., Saykally, R. J., et al. 2003, Nature, 422, 500

Mélot, M. 2003, Ph.D. Thesis, CIRIL, Université de Caen

Moore, M. H., & Hudson, R. L. 2000, Icarus, 145, 282

Moudens, A., Georges, R., Goubet, M., et al. 2009, J. Chem. Phys., 131, 204312

Oba, Y., Miyauchi, N., Hidaka, H., et al. 2009, ApJ, 701, 464

Padovani, M., Galli, D., & Glassgold, A. E. 2009, A&A, 501, 619

Palumbo, M. E. 2006, A&A, 453, 903

Palumbo, M. E., Baratta, G. A., Fulvio, D., et al. 2008, J. Phys. Conf. Ser., 101, 012002

Palumbo, M. E., Baratta, G. A., Leto, G., & Strazzulla, G. 2010, J. Mo. Struct., 972, 64

Pimblott, S. M., LaVerne, J. A., Mozumder, A., & Green, N. J. B. 1990, J. Phys. Chem., 94, 489

Plante, I., & Cucinotta, F. A. 2008, New J. Phys., 10, 125020

Raut, U., Teolis, B. D., Loeffler, M. J., et al. 2007a, J. Chem. Phys., 126, 244511

Raut, U., Famá, M., Teolis, B. D., & Baragiola, R. A. 2007b, J. Chem. Phys., 127, 204713

Raut, U., Famá, M., Loeffler, M. J., & Baragiola, R. A. 2008, ApJ, 687, 1070

Rothman, L. S., Gordon, I. E., Barbe, A., et al. 2009, J. Quant. Spectr. Radiat. Transf., 110, 533

Rowland, B., & Devlin, J. P. 1991, J. Chem. Phys., 94, 812

Rudd, M. E., Goffe, T. V., Dubois, R. D., Toburen, L. H., & Ratcliffe, C. A. 1983, Phys. Rev. A, 28, 3244

Rudd, M. E., Kim, Y.-K., Madison, D. H., & Gallagher, J. W. 1985, Rev. Mod. Phys., 57, 965

Seperuelo Duarte, E., Domaracka, A., Boduch, P., et al. 2010, A&A, 512, A71

Shen, C. J., Greenberg, J. M., Schutte, W. A., & van Dishoeck, E. F. 2004, A&A, 415, 203

Stevenson, K. P., Kimmel, G. A., Dohnalek, Z., Smith, R. S., & Kay, B. D. 1999, Science, 283, 1505

Wang, J. Z., Seo, E. S., Anraku, K., et al. 2002, ApJ, 564, 244

Webber, W. R., & Yushak, S. M. 1983, ApJ, 275, 391

Ziegler, J. F., Ziegler, M. D., & Biersack, J. P. 2010, Nucl. Instr. Meth. Phys. Res. B, 268, 1818